Bioorganic & Medicinal Chemistry 20 (2012) 6709–6723

Contents lists available at SciVerse ScienceDirect

Bioorganic & Medicinal Chemistry

journal homepage: www.elsevier.com/locate/bmc

Dimeric Smac mimetics/IAP inhibitors as in vivo-active pro-apoptotic agents. Part II: Structural and biological characterization

Daniele Lecis [a,†], Eloise Mastrangelo [b,†], Laura Belvisi [c], Martino Bolognesi [b], Monica Civera [c], Federica Cossu [b], Michelandrea De Cesare [a], Domenico Delia [a], Carmelo Drago [d], Giacomo Manenti [a], Leonardo Manzoni [e], Mario Milani [b], Elisabetta Moroni [c], Paola Perego [a], Donatella Potenza [c], Vincenzo Rizzo [d], Cinzia Scavullo [f], Carlo Scolastico [d], Federica Servida [f], Francesca Vasile [c], Pierfausto Seneci [c,d,*]

[a] Dipartimento di Oncologia Sperimentale e Medicina Molecolare, Fondazione IRCCS Istituto Nazionale dei Tumori, Via Amadeo 42, Milan I-20133, Italy
[b] Dipartimento di Bioscienze e CNR-IBF, Università degli Studi di Milano, Via Celoria 26, Milan I-20133, Italy
[c] Dipartimento di Chimica, Università degli Studi di Milano, Via Golgi 19, Milan I-20133, Italy
[d] CISI scrl, Via Fantoli 16/15, Milan I-20138, Italy
[e] Istituto di Scienze e Tecnologie Molecolari (ISTM), Consiglio Nazionale delle Ricerche (CNR), Via Golgi 19, Milan I-20133, Italy
[f] Fondazione Matarelli, Dipartimento di Farmacologia, Chemioterapia e Tossicologia Medica, Università degli Studi di Milano, Via Vanvitelli 32, Milan I-20129, Italy

ARTICLE INFO

Article history:
Available online 24 September 2012

Keywords:
IAP inhibitors
Smac mimetics
Apoptosis
In vitro profiling
Structural studies
In vivo testing

ABSTRACT

Novel pro-apoptotic, homodimeric and heterodimeric Smac mimetics/IAPs inhibitors connected through head–head (**8**), tail–tail (**9**) or head–tail linkers (**10**), were biologically and structurally characterized. In vitro characterization (binding to BIR3 and linker-BIR2–BIR3 domains from XIAP and cIAP1, cytotoxicity assays) identified early leads from each dimer family. Computational models and structural studies (crystallography, NMR, gel filtration) partially rationalized the observed properties for each dimer class. Tail–tail dimer **9a** was shown to be active in a breast and in an ovary tumor model, highlighting the potential of dimeric Smac mimetics/IAP inhibitors based on the N-AVPI-like 4-substituted 1-aza-2-oxo-bicyclo[5.3.0]decane scaffold as potential antineoplastic agents.

1. Introduction

In the preceding article[1] we described the rational design, the synthesis and the analytical characterization of Smac mimetics/IAPs inhibitors. They include head–head (**8a–i**, Fig. 1) and tail–tail homodimers (**9a–g**, Fig. 2), and heterodimeric head–tail compounds (**10a–d**, Fig. 3). Several 4-substitutions on the 1-aza-2-oxo-bicyclo[5.3.0]decane scaffold were introduced, and connecting linkers with varying flexibility and lipophilicity were used. Detailed experimental protocols leading to 20 homo- and heterodimers were described.

Here we report the cell-free binding affinity of each dimer **8–10** to the BIR3 domain—primary binding site—of XIAP and cIAP-1, and to the linker-BIR2–BIR3 construct of XIAP. Some considerations were made with regard to the head- or tail-connection between monomer units, the structure of the connecting linker, and of 4-substituents in homodimers **9** and heterodimers **10**. The cytotoxic activity of each dimer on MDA-MB-231 tumor cell lines was measured, and some factors likely to influence cellular potency were underlined. Lead compound **9a** was selected and tested in vivo. Its PK—iv and ip, healthy mice—and preliminary pharmacological profile—ip, MDA-MB-231 and IGROV-1 xenograft murine models—showed the potential usefulness of **9a** as an antineoplastic agent.

We also report the characterization of some homodimers **8** and **9**, through computational analysis, NMR, X-ray, SAXS and gel filtration experiments. The structural characterization of heterodimers **10** is ongoing, and will be reported in due time.

2. Cell-free binding to XIAP and cIAP-1 constructs

(Fig. 4) and compounds **8a**–**10d** were tested in vitro for binding to the monofunctional BIR3 domain of XIAP and ciap-1, and to the bifunctional linker-BIR2–BIR3 construct of XIAP. Two reported assay formats[4,5] were used. Calculated IC_{50} values are reported in Table 1. Minor discrepancies between our data and published binding values for standard compounds **5** and **7** are due to different environmental parameters and to calculation methods, as discussed in details elsewhere.[6]

* Corresponding author. Tel.: +39 0250314060; fax: +39 0250314075.
E-mail address: pierfausto.seneci@unimi.it (P. Seneci).
† These authors have equally contributed to the work presented here.

0968-0896/$ - see front matter © 2012 Elsevier Ltd. All rights reserved.
http://dx.doi.org/10.1016/j.bmc.2012.09.041

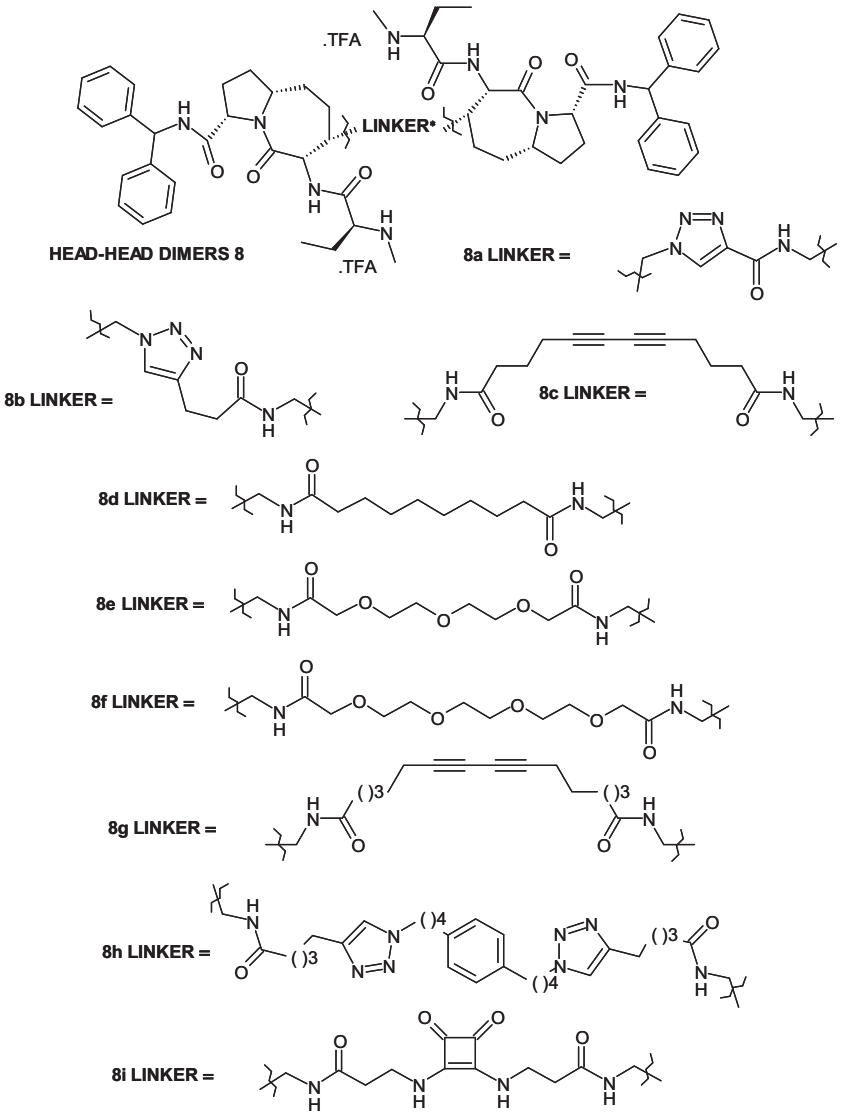

Figure 1. Structure of head–head homodimers **8a**–**i**.

Dimers **8a**–**10d** are potent inhibitors of the IAP constructs—columns 2–4, Table 1. They showed a significantly better IC_{50} value on cIAP-1 BIR3 and on the XIAP linker-BIR2–BIR3 construct, when compared to XIAP BIR3. A similar cIAP-1 vs XIAP preference was observed for structurally similar Smac mimetics.[7,8] The potent bifunctional interaction of dimers with the primary—BIR3—and secondary—linker-BIR2—Smac binding sites of XIAP is also known.[2,9]

Tail–tail homodimers **9** and head–tail heterodimers **10** showed a similar binding profile. Homodimers **9a–e**, **9g** and heterodimers **10a–c** showed IC_{50} values between 24.5 and 31.2 nM on XIAP BIR3, between $\leqslant$1 and 5.4 nM on cIAP-1 BIR3, and $\leqslant$1 nM on the linker-BIR2–BIR3 construct from XIAP. Tail–tail dimer **9f** was slightly less potent—IC_{50} = 65.7 nM on XIAP BIR3, IC_{50} = 17.6 nM on cIAP-1 BIR3, and IC_{50} = 4.37 nM on XIAP linker-BIR2–BIR3. Heterodimer **10d** was less potent on XIAP—IC_{50} = 293 nM on XIAP BIR3, IC_{50} = 5.3 nM on XIAP linker-BIR2–BIR3, but retained an IC_{50} $\leqslant$1 nM on cIAP-1 BIR3.

As to homodimers **9a–g**, the linker did not influence their cell-free potency on XIAP BIR3, confirming that pro-R phenyl replacement in the diphenylamide moiety is tolerated.[10] Dual binding of tail–tail dimers **9** to the conformationally flexible XIAP linker-BIR2–BIR3 construct was also linker-independent. 4-Substitution with unhindered hydroxymethyl—**9a**–**9e**—and 2-aminoethyl groups—**9g**—established a hydrogen bond between the 4-substituent and Thr308–Asp309 residues in XIAP.[6] The bulky 4-benzylaminomethyl group—**9f**—may slightly weaken the same hydrogen bond interaction for steric reasons.

Heterodimers **10a–c** showed an affinity profile similar to tail–tail dimers **9a–e**. We suggest an interaction with XIAP BIR3 through the tail-linked, 4-hydroxymethyl-substituted monomeric unit in **10a**–**c**—favored by hydrogen bond interactions with Thr308/Asp309. We suggest the same initial, rate-limiting binding step between the tail-linked monomeric unit in **10a–c** and the BIR3 domain in the linker-BIR2–BIR3 construct. A subsequent intramolecular binding of the head-linked monomeric unit to the secondary BIR2 binding site is rate- and potency-irrelevant. Thus, the binding strength for 4-hydroxymethyl-substituted dimers **9a–e** and **10a–c** is similar.

Hybrid heterodimer **10d** showed a lower XIAP BIR3 affinity, possibly due to the absence of a hydrogen bond interaction with Thr308/Asp309 residues. The initial **10d**-BIR3 contact within the linker-BIR2–BIR3 construct may happen through either monomeric unit, followed by the second, intramolecular interaction with

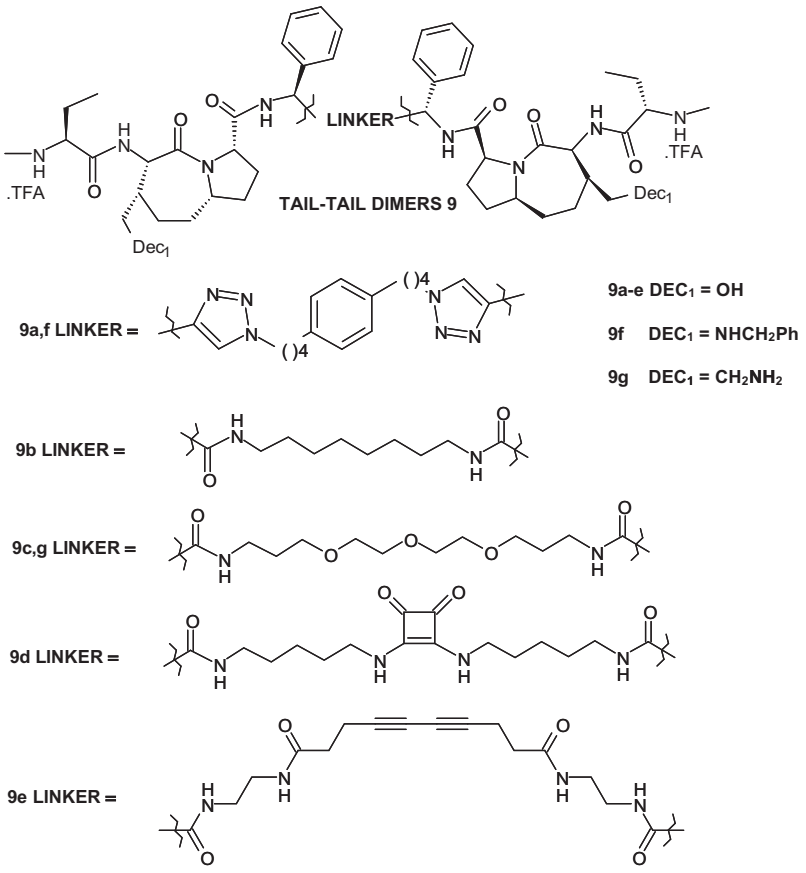

Figure 2. Structure of tail–tail homodimers **9a**–**g**.

BIR2. The observed IC_{50} reduction mirrored the lower affinity of heterodimer **10d** in the first, rate-limiting binding event.

Head–head homodimers **8** showed some variability in terms of cell-free binding. As to XIAP, they were less potent than dimers **9** and **10**, once more possibly due to the absence of a hydrogen bond interaction with Thr308/Asp309 residues. A limited linker-dependent SAR was observed, with a XIAP BIR3 IC_{50} range between 352 and 37.5 nM, and with a linker-BIR2–BIR3 IC_{50} range between 16.2 and 1.6 nM.

Head–head dimers **8** were as potent cIAP-1 BIR3 binders as dimers **9** and **10**—IC_{50} between $\leqslant$1 and 3.8 nM. The absence of binding interactions involving 4-substituents within cIAP-1 BIR3 may justify the same binding potencies for dimers **8–10**.

Limited SAR considerations can be made for dimers **8**. The shortest linkers in compounds **8a, b** may cause their slightly reduced binding on mono- and bifunctional XIAP constructs. Oxygen-containing linkers in dimers **8e, f** had a slightly detrimental effect on linker-BIR2–BIR3 binding compared with the sp3 carbon-containing linker in compound **8d**, possibly due to lipophilic regions in the BIR2–BIR3 interface of XIAP. The squarate-connected dimer **8i** showed the best affinity for any XIAP and cIAP-1 construct, suggesting an active participation of the linker in binding interactions with the BIR domains.

Standard dimer **7**[3] showed a comparable binding profile with its close congener **9a**. A small reduction in potency on XIAP BIR3and a small increase in potency on cIAP-1 BIR3, were observed. Standard dimer **5**[2] displayed good potency on both XIAP constructs, and a lower affinity for cIAP-1 BIR3. We may suggest that hybrid compound **10d** could strongly bind to cIAP-1 BIR3—IC_{50} $\leqslant$1 nM—through its **8**-like 1-aza-2-oxobicyclo[5.3.0]decane monomeric unit, as binding through its **5**-like portion should lead to a weaker interaction.

Finally, we attempted to identify inter- and intra-class structural variations by measuring their influence on the binding ratio for mono- and bifunctional XIAP constructs (C2/C4, column 5, Table 1). We calculated such ratios using the observed IC_{50} for each dimer.

The binding ratio for mono- and bifunctional XIAP constructs should provide information on the tendency of compounds **8**–**10** to behave as 'true dimers'. We reasoned that higher ratios should characterize strong bifunctional ligands, while lower ratios may indicate some hindrance limiting the intramolecular BIR2–BIR3 interaction of a given dimer.

Observed C2/C4 ratio showed a limited variability, ranging between 7.4 and 78.2. As IC_{50} values are approximated, though, we do not consider the observed, limited variability as adequate to establish a reliable inter- or intra-class SAR.

3. Cytotoxicity against tumor cell lines

Due to their sub-micromolar activity in cell-free assays, both literature standards and our twenty dimers were tested for their cytotoxicity. MDA-MB-231 cells, a breast cancer cell line which has repeatedly been used to test Smac mimetics/XIAP inhibitors, were selected. Measured IC_{50} are reported in Table 2.

As the compounds were tested throughout several years, we used two different batches of MDA-MB-231 cells. A slightly different cytotoxic activity of reference standard **7** and tail–tail dimer **9a** on the two batches was observed (Table 2). We believe that this does not prevent us from extracting a preliminary cellular structure–activity relationship for dimers **8**–**10**.

We observed a decrease in cellular vs cell-free potency for dimers **8–10.** The ratio between cellular cytotoxicity and cell-free

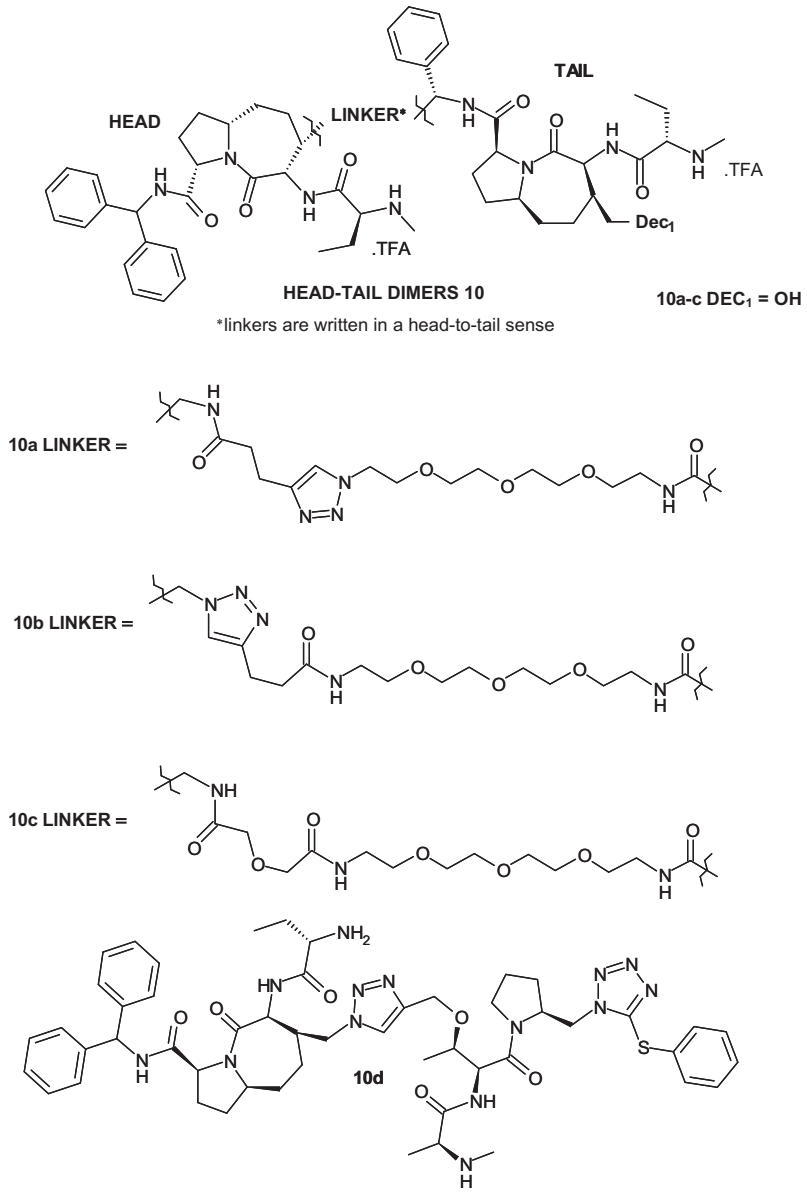

Figure 3. Structure of head–tail heterodimers **10a**–**d**.

potency—ratio C2/C5, column 6, Table 2—was class- and structure-dependent. Bivalent, high molecular weight compounds are known to encounter difficulties in reaching their intracellular targets.[12] Structurally related, dimeric Smac mimetics recently showed a correlation between MDA-MB-231 cytotoxicity and cell permeability.[13]

Head–head dimers **8** showed cytotoxicity on MDA-MB-231 cells between 337 nM and 4.84 μM. Oxygen-containing linkers in **8e, f** slightly decreased their C2/C5 ratio up to ~30, compared with values between 100 and 700 for other head–head dimers **8**. We suggest that monomeric units connected through their 4-substituents are extremely lipophilic, that the hydrophilic linkers in **8e, f** balance their partition coefficient and make them slightly more cell permeable. Recently, 5-connected head–head homodimers based on a structurally related decahydropyrrolo-1,5-diaza-6-oxo diazocine scaffold were reported.[9] As their cell-free potency is comparable with our dimers **8**, their low nanomolar cytotoxicity on MDA-MB-231 cells is probably strongly influenced by a better physico–chemical profile.

Tail–tail dimers **9** showed the larger variations in cellular potencies, between 55 nM and >50 μM. Compounds **9a, b, f** showed nanomolar cytotoxicity, with **9a** being the most cytotoxic among our entire dimer set. Compounds **9c–e** displayed weak cellular potency, while **9g** was inactive.

The cellular inactivity of **9g** may be explained by its positively charged 2-aminoethyl 4-substitution, preventing dimer penetration through the lipophilic cell membrane. The 4-hydroxymethyl substituent in tail–tail dimers **9a–e** did not prevent their cell penetration, and the observed differences in cytotoxicity among them are attributed to their linkers. The known triazole-based linker[10] determined the best cellular potency and C2/C5 ratio in **9a**, and comparable values for **9f**. Sub-micromolar potency was shown by **9b**, containing a short hydrophobic linker. Dimers **9c–e** showed a drop in cytotoxicity, and higher C2/C5 ratios. Recently, 4-unsubstituted tail–tail dimers based on aza-2-oxobicycloundecane scaffolds showed a correlation between linker structure, cell-free and cellular activities.[13] This correlation may be partially applicable to our 4-substituted tail–tail dimers **9a–g**.

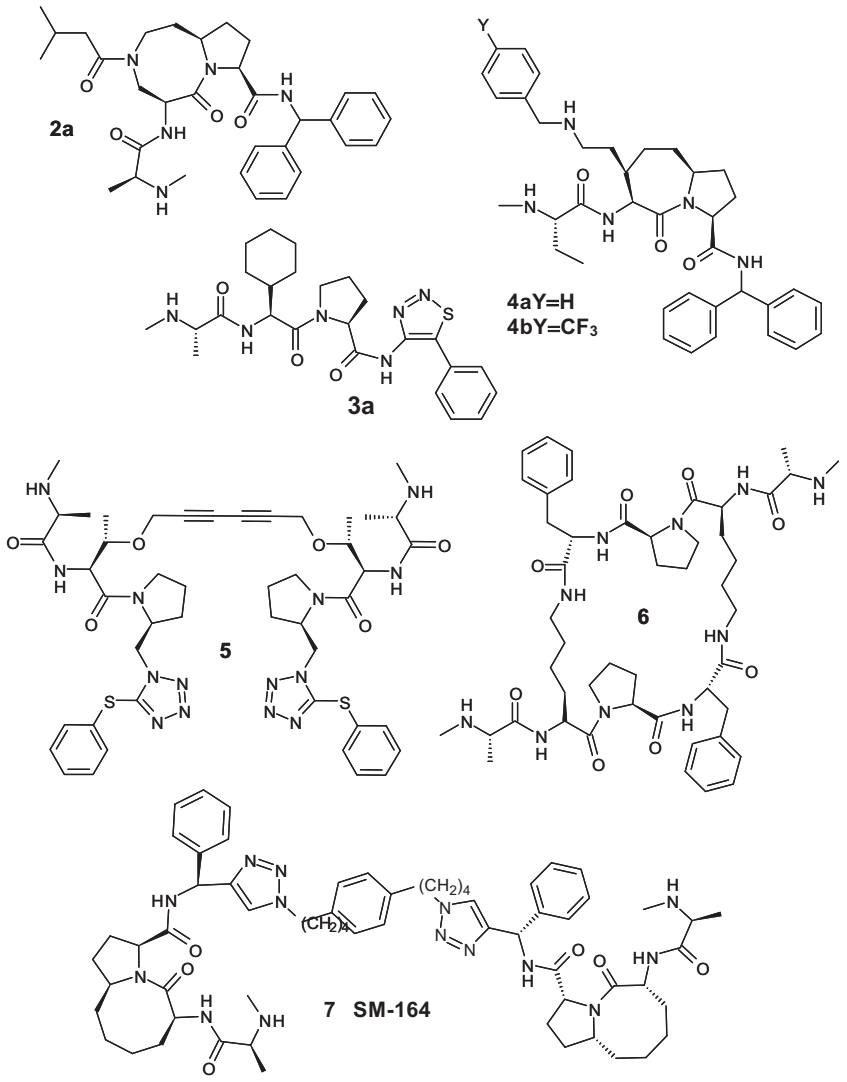

Figure 4. Previously reported monomeric and dimeric Smac mimetics/IAP inhibitors.

Table 1
IC_{50} of compounds **5**, **7**, **8a**–**10d** on XIAP BIR3, cIAP-1 BIR3, and XIAP l-BIR2–BIR3

Compound/Smac	IC_{50}, BIR3 XIAP[a]	RSD (%)	IC_{50}, BIR3 cIAP-1[a]	RSD (%)	IC_{50}, l-BIR2–BIR3 XIAP[a]	RSD (%)	Ratio C2/C4
5	80.7	10	12.6	16	3.3	18	24.5
7	41.2	16	⩽1	23	⩽1	25	⩾41.2
8a	244	15	1.7	9	15.5	18	15.7
8b	352	11	2.9	12	8.4	16	41.9
8c	305	20	1.4	10	3.9	18	78.2
8d	181[b]	13	1.4	25	5.9[b]	22	30.7
8e	125	6	1.7	12	15.5	27	8.1
8f	120	6	⩽1	14	16.2	21	7.4
8g	179[b]	16	3.8	23	3.2[b]	18	55.9
8h	157[b]	14	3.5	21	2.3[b]	25	68.3
8i	37.5	5	⩽1	14	1.6	38	23.4
9a	25.4	11	5.4	12	⩽1	25	⩾25.4
9b	29.9	13	1.9	12	⩽1	22	⩾29.9
9c	26.0	14	1.5	17	⩽1	18	⩾26.0
9d	26.7	16	2.6	11	⩽1	18	⩾26.7
9e	24.5	12	1.1	18	⩽1	18	⩾24.5
9f	65.7	8	17.6	12	4.4	22	14.9
9g	24.9	13	⩽1	21	⩽1	16	⩾24.9
10a	31.2	29	1.5	5	⩽1	5	⩾31.2
10b	29.7	29	5.0	17	⩽1	17	⩾29.7
10c	31.1	31	3.2	10	⩽1	10	⩾31.1
10d	293	16	⩽1	33	5.3	16	55.3

[a] nM.
[b] Previously published data, see Ref. 11.

Table 2
IC_{50} of compounds **5**, **7**, **8a**–**10d** on tumor cell lines

Compound/Smac	IC_{50} MDA-MB-231[a]	IC_{50} HL-60[a]	IC_{50} PC-3[a]	IC_{50}, l-BIR2–BIR3 XIAP[b]	Ratio C2/C5
5	*0.175 ± 0.042*[c]			3.3	53.0
7	0.039 ± 0.008/*0.006 ± 0.00004*			⩽1	⩾39
8a	*4.84 ± 0.8*	7.39 ± 0.048	>50	15.5	312.3
8b	*3.32 ± 0.75*			8.4	395.2
8c	*0.728 ± 0.033*			3.9	186.7
8d	ND[d]			5.9	–
8e	*0.379 ± 0.006*	0.935 ± 0.016	>50	15.5	24.5
8f	*0.567 ± 0.06*			16.2	35.0
8g	*0.337 ± 0.04*	0.128 ± 0.04	>50	3.2	105.3
8h	*1.60 ± 0.248*			2.3	695.7
8i	*2.30 ± 0.173*			1.6	1438
9a	0.055 ± 0.00097/*0.162 ± 0.024*	0.071 ± 0.05	>50	⩽1	⩾55
9b	0.540 ± 0.261			⩽1	⩾540
9c	46.9 ± 1.9			⩽1	⩾46,900
9d	45.4 ± 6.48			⩽1	⩾45,400
9e	*10.6 ± 0.248*			⩽1	⩾10,600
9f	0.430 ± 0.158			4.4	97.7
9g	>50			⩽1	>50,000
10a	10.7 ± 0.039	20.6 ± 11.3	>50	⩽1	⩾10,700
10b	*1.28 ± 0.006*			⩽1	⩾1280
10c	*0.582 ± 0.029*			⩽1	⩾582
10d	*3.28 ± 0.184*			5.3	618.9

[a] μM.
[b] nM.
[c] IC_{50} values in italics were determined using a different MDA-MB-231 cell line.
[d] Not determined, due to compound insolubility.

Cell-free potent heterodimers **10a–d** suffered a large potency decrease on MDA-MB-231 cells, with cytotoxicity between 582 nM and 10.7 μM and large C2/C5 ratios. The limited number of prepared heterodimers **10** could not lead to any substantiated structure–activity consideration.

Five dimers were tested for cytotoxicity on the Smac mimetic-sensitive promyelocytic leukemia HL60 cell line (column 3, Table 2), and on the Smac mimetic-refractory prostate cancer PC-3 cell line (column 4, Table 2). Compounds **8a**, **8e, 8g**, **9a** and **10a** were inactive against the latter cells, as expected. The cytotoxicity of the five tested dimers on HL60 cells was broadly similar to their cytotoxicity against MDA-MB-231 cells.

As a result of in vitro biology profiling of dimers **8a**–**10d**, we selected **9a** as an early dimer lead, and we tested it on suitable in vivo models—vide infra—using **7** as a reference standard.

4. Computational studies

Head–head dimer **8e** and tail–tail dimer **9a** were selected as representatives for their families. Computational models for their binding to the linker-BIR2–BIR3 construct of XIAP were built by means of extensive molecular dynamics (MD) simulations, using the high resolution crystal structures available in Protein Data Bank[14] for BIR2 and BIR3 domains. Taking into account protein and ligand flexibility, these studies can complement the structural characterization obtained by nMR and crystallographic experiments—vide infra. They provided a dynamic view of ligand–receptor interactions and disclosed the molecular basis of the recognition of head–head (**8**) or tail–tail (**9**) dimeric Smac mimetics by the linker-BIR2–BIR3 construct from XIAP at the atomic level.

Following the procedure described in the Experimental section, three-dimensional structures of a multi-domain XIAP construct (residues 127–345) in complex with the head–head dimer **8e** or the tail–tail dimer **9a** were built. The crystal structure of the cyclic, bivalent Smac mimic **6** in complex with the XIAP BIR3 domain (PDB entry 2VSL)[15] and the crystal structure of the XIAP BIR2 domain in complex with caspase 3 (PDB entry 1I3O)[16] was used as a model. Finally, both **8e**/**9a**—multi-domain XIAP construct structures were refined and investigated through extensive explicit solvent MD simulations using the Amber software suite.[17]

In the modelled starting structures, the distance between the centers of mass for BIR2 and BIR3 domains is about 28 Å. This is due to the restraint imposed by the cyclic bivalent Smac mimic **6** on the intermolecular crystallographic XIAP-BIR3 dimer used as template for the linker-BIR2–BIR3 structure generation. The analysis of MD trajectories revealed some conformational changes for both the ligand and the protein in our structures.

Both the head–head and tail–tail linker of **8e** and **9a** relaxed some strain affecting the initial conformations of the complexes. A mutual ligand-receptor structural adjustment, as well as the reorganization of the ligand-protein interaction network (in a complexed state) were achieved. Distance values between the centers of mass of BIR2 and BIR3 domains were thus adjusted in the 30–32 Å range for the simulation with compound **8e**, and in the 31–34 Å range with compound **9a**. However, compact structures of the bifunctional protein construct were maintained, allowing the dimeric Smac mimetics **8e** and **9a** to behave as bivalent ligands able to simultaneously bind to XIAP BIR2 and BIR3 domains.[18] In

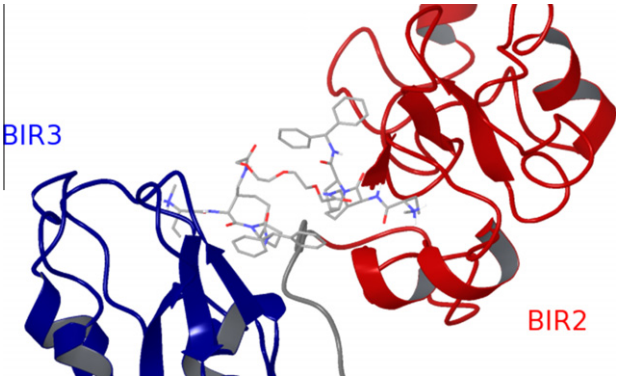

Figure 5. A snapshot from the MD simulation of **8e** (tube representation, C atoms in gray, N in blue and O in red) in the linker-BIR2–BIR3 construct (red and blue ribbon representation).

particular, the network of protein/ligand interactions displayed by the N-terminal tetrapeptide sequence of Smac[19] (and several monovalent Smac mimetics)[6,20] in the BIR3 IBM pocket was conserved throughout the MD simulations of the complexes for both the AVPI-related recognition subunits of the dimeric Smac mimetics.

In details, analysis of the trajectories showed that one peptidomimetic subunit interacted with the BIR3 domain, forming intermolecular hydrogen bonds with Gly306, Thr308, Asp309, Glu314, Gln319, and Trp323. Concurrently the other subunit established the same intermolecular hydrogen bond pattern with the BIR2 residue, corresponding to a structure-based alignment of the amino acids in the IBM groove of the BIR2 and BIR3 domains of XIAP (Lys206, Lys208, Asn209, Asp214, Glu219, His223). Similar binding modes to both BIR domains were observed in our computational studies on 4-substituted 1-aza-2-oxobicyclo[5.3.0]decane monomeric Smac mimetics,[21] likely due to the high degree of sequence and structural homology of the IBM groove in the BIR2 and BIR3 domains.

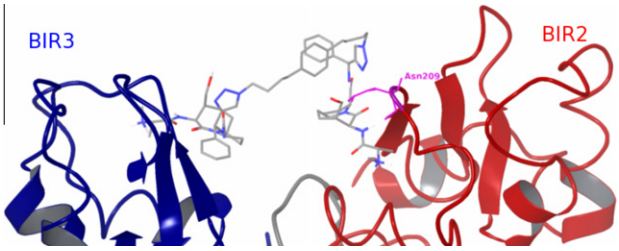

Figure 6. A snapshot from the MD simulation of **9a** (tube representation, C atoms in gray, N in blue and O in red) in the linker-BIR2–BIR3 construct (red and blue ribbon representation). Asn209 residue is shown as pink tube representation.

The analysis of the MD trajectory of the head–head dimer **8e** revealed a symmetrical arrangement of the two AVPI peptidomimetic motifs in the BIR domains, characterized by almost identical H-bond patterns and Van der Waals contacts (Fig. 5).

On the contrary, the rotation of two torsions (Pro psi and torsion centered at NH16–CH15 bond) at the C-terminus amide 'tail' of the ligand subunit interacting with BIR2 was observed throughout the MD simulation of the tail–tail dimer **9a**. These torsional changes resulted in the loss of an H-bond between the phenylamido proton NH16 and the BIR2-Lys206 carbonyl group, and in the modified interaction pattern involving the ligand linker moiety and the BIR2 domain. Consequently, the two AVPI peptidomimetic motifs of the dimer **9a** showed simultaneous but slightly different binding with the BIR2 and BIR3 domains (Fig. 6). In particular, the terminal phenyl group of the BIR3-addressing subunit is located into a hydrophobic pocket formed by the side chains of Leu292, Lys297, Val298, and Lys299, while the triazole ring close to the same ligand subunit is exposed to solvent, forming only few contacts with the BIR3–Tyr324 residue. Conversely, due to previously described torsional rotation, the terminal phenyl group of the BIR2-addressing subunit left the hydrophobic pocket during the simulation, while the neighboring triazole ring approached the BIR2 binding site forming favourable Van der Waals contacts especially with the Lys206, Lys208 and Asn209 residues. Stabilizing H-bond interactions were also established between Asn209 side chain donor hydrogens and triazole acceptor nitrogens in almost 40% of the sampled structures.[22]

Finally, as far as the phenyl group located at the centre of the tail–tail linker of **9a** is concerned, MD simulation revealed favourable Van der Waals contacts between the phenyl protons and the Asn209 side chain atoms, likely driven by a stacking interaction between the linker phenyl group and the BIR2-addressing triazole ring. Interestingly, the sampled structures of **9a** offer an explanation

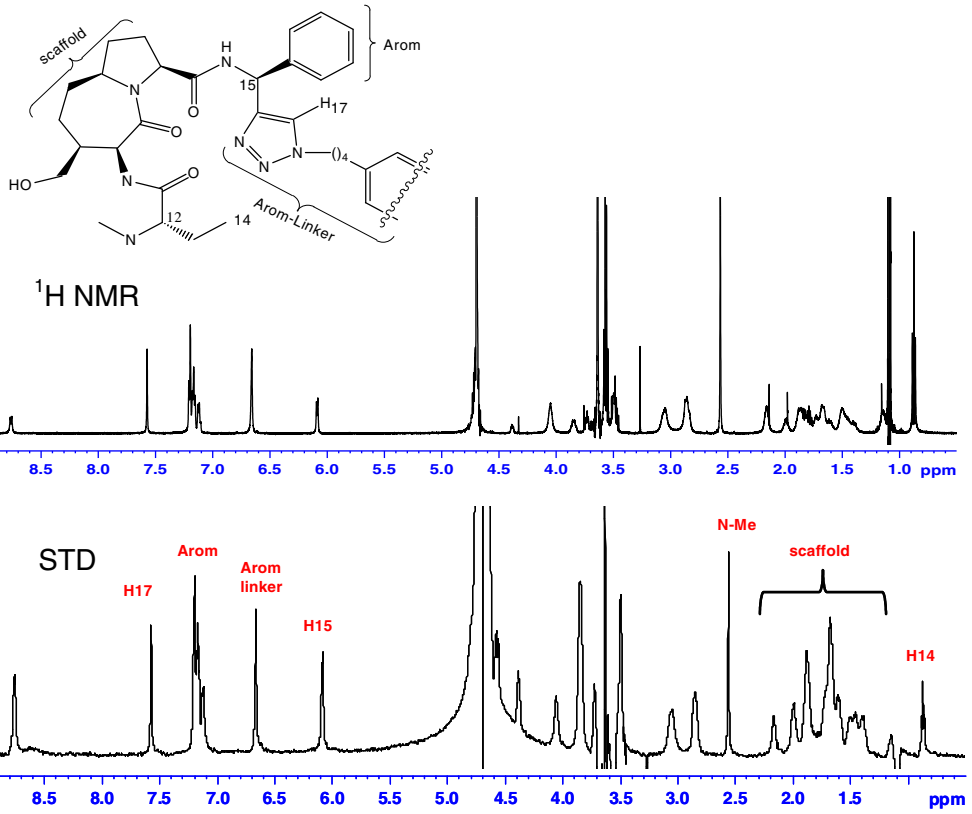

Figure 7. STD–NMR spectra of the **9a**- linker-BIR2–BIR3 complex.

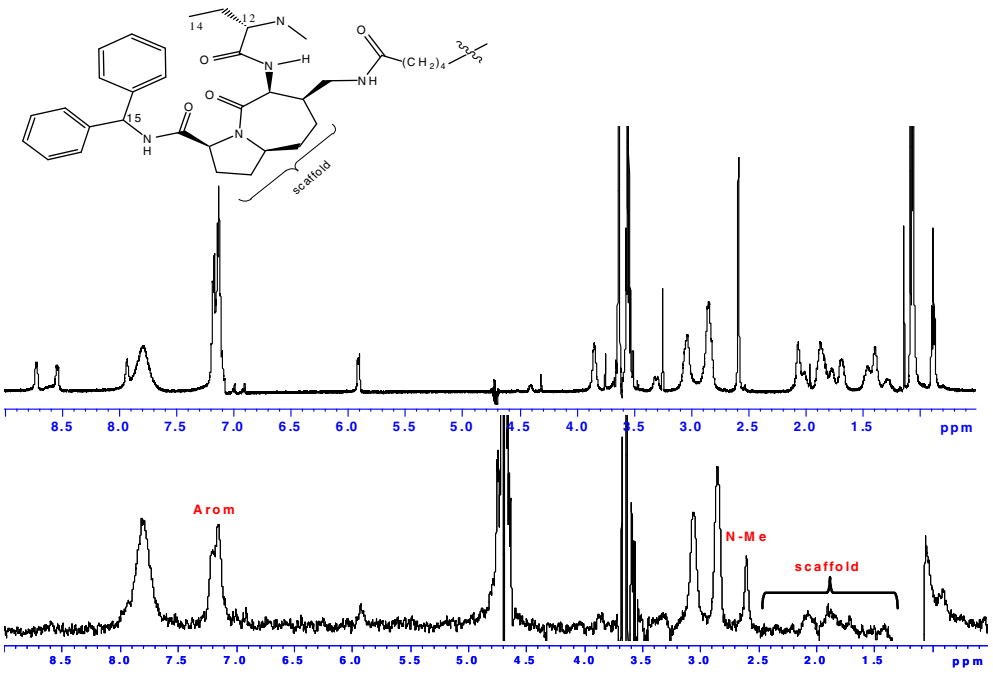

Figure 8. STD–NMR spectra of the **8d**- linker-BIR2–BIR3 complex.

of the NOE contacts experienced by ligand protons in the linker-BIR2–BIR3 construct (STD–NMR experiments, vide infra), showing favourable contacts between the aromatic protons of the core phenyl linker and Asn209 side chain protons, and between the triazole proton H17 and Lys206, Lys208 and Asn209 residues.

5. STD–NMR studies

Saturated Transfer Difference NMR (STD–NMR), together with trNOESY, is one of the most widespread NMR methods to study the interactions between small ligands and macromolecular receptors.[23] Originally proposed as a technique for the rapid screening of compound libraries, its scope has been extended to include mapping the interaction epitope(s) by determining the ligand regions in contact with a given receptor.[24] The method is based on the transfer of saturation from the protein to the bound ligand which in turn, by exchange, is moved into solution where it is detected. During the saturation period, progressive saturation transfers from protein to ligand protons when the ligand binds to the target. Ligand protons nearest to the protein are most likely to be saturated to the highest degree, and to have the strongest signal in the STD spectrum. The degree of saturation of individual ligand protons (expressed as absolute-STD percent)[22] reflects their proximity to the protein surface, and can be used as an epitope-mapping method to describe the target–ligand interactions.

We selected head–head compound **8d** and tail–tail dimer **9a** for an in-depth STD–NMR investigation of their interaction mode with the XIAP linker-BIR2–BIR3 construct. We performed a set of experiments on soluble linker-BIR2–BIR3—dimeric ligand complexes in non deuterated aqueous buffer, aiming to identify which functional groups of the ligand interact with the biological construct.

The STD spectrum of **9a** in presence of linker-BIR2–BIR3 is reported in Figure 7, bottom, together with the dimer spectrum per se, top. We observed target–ligand interactions involving the phenyl ring on C15-aromatic-7.2 ppm-1.43% degree of saturation, and H15-6.1 ppm-0.6%; the bicyclic scaffold—2.3 to 1.3 ppm-1.43%; and the ethylglycine residue—N-Me-2.6 ppm-0.7% and H14-1.4 ppm-0.53%. In addition, the aromatic protons of the linker connecting the two dimer subunits interact with the protein, showing a 1.18% degree of saturation for the core phenyl ring- 7.6 ppm -, and a 1.66% degree of saturation for the triazole proton H17-6.7 ppm. These linker-protein interactions are consistent with the computational observations described above.

The STD spectrum of **8d** in presence of linker-BIR2–BIR3 is reported in Figure 8, bottom, together with the dimer spectrum per se, top. We observed target–ligand interactions involving the diphenylmethylamide—aromatic-7.2 ppm-0.83% degree of saturation and H15-5.9 ppm-1.06%; the bicyclic scaffold—2.3 to 1.3 ppm-1.08%; and the ethylglycine residue—N-Me-2.6 ppm-1.06% degree of saturation. The connecting linker between the two dimer subunits did not show any interaction. Overall, we observed a smaller number of interactions between head–head dimer **8d** and the target, when compared with tail–tail dimer **9a**.

This, and the variations in STD–NMR degree of saturation/intensities for the same functional groups in **8d** and **9a**—see Figure 9 for a visual comparison—may indicate a different binding mode, and may justify the higher affinity for linker-BIR2–BIR3 of tail–tail dimer **9a** versus head–head dimer **8d**.

6. Crystallographic studies

Both head–head dimers **8** and tail–tail dimers **9** were studied using either mono-domain—BIR3—and multi-domain—linker-BIR2–BIR3, BIR2–BIR3—XIAP constructs. Unfortunately, as of today

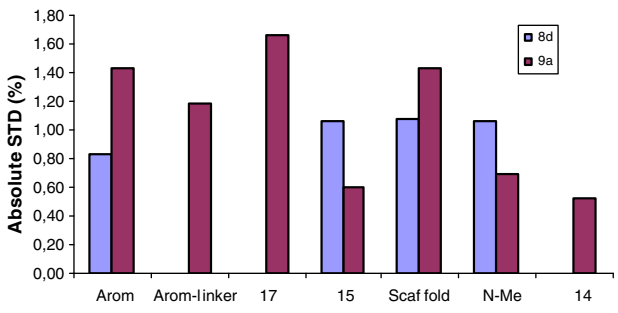

Figure 9. NMR–STD comparison between **8d** (violet) and **9a** (cyan).

we were unsuccessful in obtaining suitable crystals of complexes between any dimer and any multi-domain construct. No results were obtained also when complexes between several head–head dimers **8** and XIAP-BIR3 were targeted; the XIAP-BIR3 domain, conversely, provided good co-crystals in the presence of tail–tail dimer **9a**.

The 3D structure of this complex was solved by means of the molecular replacement method, and refined at 3.3 Å resolution, showing that ten XIAP-BIR3 molecules (per asymmetric unit) are assembled into dimers (AF, BG, CJ, DK, EL). The crystal packing achieved is different from that observed for the structures of XIAP-BIR3 in complex with monovalent Smac-mimetic compounds known to date[6,20] (PDB codes 3EYL, 3CLX, 3CM2, 3CM7). Therefore, dimerization of XIAP-BIR3 appears to be linked to the presence of **9a**. Notably, the crystal lattice packing is also different from that observed for XIAP-BIR3 in complex with standard dimer **5** (PDB code 3G76),[20] whose crystal asymmetric unit hosts eight BIR3 molecules and eight molecules of **5**, each of which has an inhibitory head bound to BIR3 and the other devoid of any contacts to the protein. Thus, we argue that **9a** is a better bivalent binder than **5**—as observed from cell-free binding data -, as it induces an intermolecular dimerization of XIAP-BIR3.

In details, **9a** heads bind to XIAP-BIR3 between the β3 strand and the α3 helix, in a region roughly lined by residues Gly306, Thr308, Asp309, Lys311, Glu314 and Trp323 (Fig. 10), consistent with computational predictions. Electron density is available also for the phenyl group located at the centre of the connecting linker, joining the two subunits of **9a**. So far, within bivalent Smac-mimetic compounds reported by the literature,[2,3,10] the linker segment has not been implicated in any BIR recognition mechanism, while both our computational predictions—albeit mostly with the BIR2 domain—and STD–NMR data confirm this observation. It can be noticed that the linker in **9a** participates in hydrophobic contacts (Fig. 10) that do not appear to influence recognition of the BIR pocket by the Smac-mimetic. In particular, the triazole ring lays between Tyr324, in the α3 helix, and Asn249, or Arg248, in the N-terminal region. We stress that **9a** linker-BIR interactions were observed with both STD–NMR and crystallography, and that were attributed to the same linker regions.

Further structural insights may be obtained through the characterization of other dimer (including heterodimers **10**)—target (including multi-domain constructs from XIAP and cIAP-1) complexes. Such results will be reported in due time.

7. Gel filtration and SAXS

In order to estimate the simultaneous interaction of homo-dimer compounds **8** and **9** with XIAP-BIR2–BIR3 domains in solution, we performed analytical gel filtration assays. The chromatograms obtained for XIAP-BIR2–BIR3 in presence of **8c**, **8d**, **8g**, **8h**, **9a**, and **9c** show a shift of the elution volume (Ve, 11.0 mL for XIAP-BIR2–BIR3 alone) to higher values for all tested dimers (Ve = 11.3 mL for XIAP-BIR2–BIR3 in presence of **8d** and **8h**, 11.4 mL in presence of **8c**, **8g**, **9a** and **9c**). This suggests similar conformational changes with an actual reduction of the protein volume. A more compact protein structure may be explained by a conformational change induced by simultaneous binding of two subunits contained in each homo-dimer to the two domains of the bifunctional construct, as confirmed by the SAXS data obtained for compound **9a**.

The two solution scattering patterns of XIAP-BIR2–BIR3 in the absence/presence of **9a** exhibit significant differences, showing that inhibitor binding causes a global conformational change of the protein.[25] In particular, Guinier plot analysis of the two curves shows a reduction of the radius of gyration in the presence of the ligand compound from 25.0 ± 0.2 Å to 20.7 ± 0.2 Å. Such values point toward a major conformational transition of XIAP-BIR2–BIR3, from an extended to a more compact conformation upon inhibitor binding, as already observed by us with the dimeric standard **5**.[20]

8. Lead selection for in vivo studies

Dimeric compounds **8a**–**10d** have a sub-optimal 'drug-like' profile, needed for a bifunctional interaction with IAP proteins, with respect to monomeric compounds **2a**–**4b** (Fig. 4). In particular, their molecular weight exceeds 1000 Dalton, and their physico–chemical properties are likely to be unsuitable for oral administration.[26] Thus, iv and i.p administration routes were considered, in accordance with recent publications for similar dimeric Smac mimics.[9,13,27]

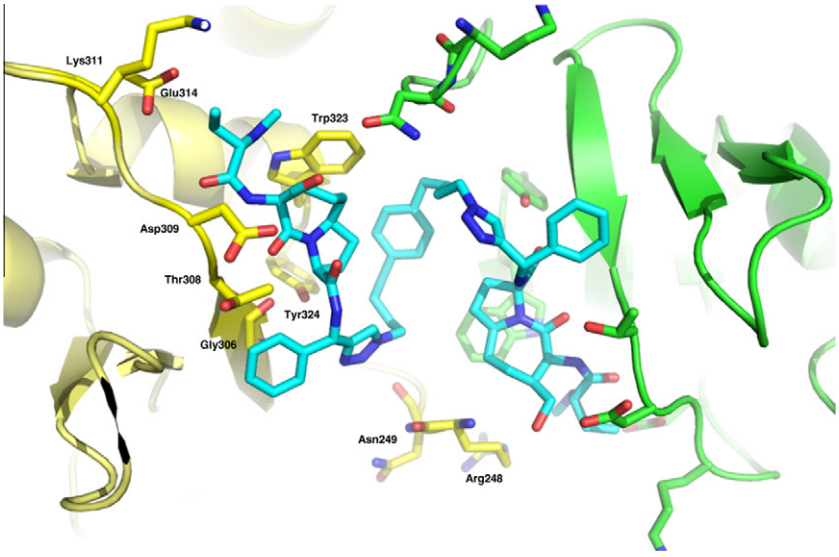

Figure 10. Molecules A (yellow) and F (green) in the X-ray structure of XIAP-BIR3 in complex with **9a** (light blue). The amino acids involved in the interaction with **9a** are showed as sticks (for simplicity only amino acids of the molecule A are labelled).

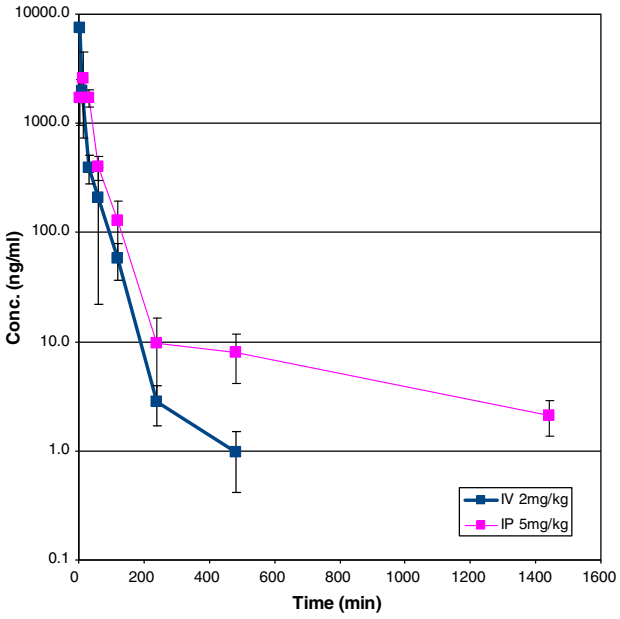

Figure 11. PK profiles for **9a** after iv – cyan – and ip – magenta – administration.

As previously mentioned, we selected the early dimer lead **9a** as possessing the best cell free-cellular potency profile, and we studied its in vivo behavior. We reasoned that its early pharmacokinetic and in vivo efficacy profiling would hopefully have provided us with more information on chemical class liabilities, and would have given us the opportunity to design more appropriate structures for further in vivo testing.

9. Pharmacokinetic evaluation of 9a

Homodimer **9a** was administered iv (2 mg/Kg, in 0.9% NaCl) and ip (5 mg/Kg, in 0.9% NaCl) to fed male CD-1 mice (24 mice cohort). Plasma levels of **9a** were determined at 8 time points during 24 h post administration. No adverse behavioural effects were noted during the treatments. The comparison of iv and ip profiles for **9a** is shown in Figure 11.

Compound **9a** showed a low clearance (20 mL/min/kg) after iv administration with a mean residence time—MRT—of 20 min. The $T_{1/2}$ of the elimination phase was calculated as 51 min, but is likely to be underestimated because extracted from the entire curve—up to 24 h, although the last point could not be quantified (below the lower limit of quantification, LLOQ).

Compound **9a** was rapidly absorbed after ip administration, with a C_{max} of 2608 ng/mL at 15 min. The MRT was determined as 69 min. The $T_{1/2}$ of the elimination phase was calculated as 185 min, and the compound was quantified up to 24 h. Compound **9a** showed a good bioavailability after ip administration (around 49%).

Overall, measured pharmacokinetic properties of the early lead **9a** were deemed suitable for ip administration in a suitable oncology mouse model.

10. Efficacy evaluation of 9a

We selected two tumor models, respectively on the basis of the 'gold literature standard' MDA-MB-231 breast cancer model[3] for Smac mimetics, and of our own expertise using an human ovarian carcinoma model (IGROV-1) adapted to grow in the peritoneal cavity (ip) and subcutaneously (sc).[27,28]

As to the former model, anti-tumour activity studies were carried out using the human breast cancer cell line MDA-MB-231 injected subcutaneously in NOD/SCID mice. When treated with compound **9a** (ip, 5 mg/Kg, qdx5/wx3), a significant inhibition of tumor growth was observed (TVI being of 63%, P <0.05 vs controls). Moreover, neither body weight loss, nor lethal toxicity were observed, supporting the idea that the compound is well tolerated at the dose administrated.

As to the latter model, mice xenografted ip with IGROV-1 human ovarian carcinoma cells were injected ip with compound **9a** or standard dimer **7**, both delivered qd4-5/wx2 at a dose of 5 mg/kg. Treatment started the day after tumor cell inoculation. The ip delivery of compound **9a** led to a significant increased survival time compared with controls (P <0.05) with a T/C value of 180%. Using the same dose and with the same schedule as compound **9a**, the T/C value obtained using standard dimer **7** was 164% (P <0.05). Thus, although the tail–tail dimer **9a** appeared slightly superior to standard **7** in this experimental setting, both compounds were endowed with antitumor activity on the ip IGROV-1 tumor.

When mice were xenografted sc with IGROV-1 in another experimental setting,[27] a significant inhibition of tumor growth was observed with compound **9a** administration (ip, 5 mg/Kg, qdx5/wx3), the TVI being of 66% (P <0.05 vs controls). In contrast, under the same experimental conditions standard **7** did not display any antitumor effect. Both compounds were well tolerated, judging from the lack of any significant body weight loss, and of lethal toxicity.

Lead compound **9a** showed only marginal cytotoxicity against IGROV-1 cells at 20 μM. Its gain of activity in vivo, and the different activity profile of **9a** and **7** on IGROV-1 xenograft models, is

Table 3
Efficacy of **9a** (MDA-MB-231, IGROV-1) and **7** (IGROV-1) on the breast cancer MDA-MB-231 injected subcutaneously (sc) in NOD/SCID mice, on the ovarian carcinoma IGROV-1 xenografted in the peritoneal cavity (ip) or injected sc in athymic nude mice[a]

Tumor model, growth site	Dimer	T/C[b] (%)	P[c]	TVI[d] (%)	BWL[e] (%)	tox[f]	P[g]
MDA-MB-231, sc	**9a**			63	—	0/8	0.019
IGROV-1, ip	**9a**	180	0.0001				
IGROV-1, ip	**7**	164	0.0007				
IGROV-1, sc	**9a**			66	2	0/8	0.034
IGROV-1, sc	**7**			0	5	0/8	n.s.[h]

[a] Compound **9a** (ip, 5 mg/Kg) and **7** (ip, 5 mg/Kg) were compared as detailed in the Experimental section.
[b] % of median survival time in treated athymic nude mice, compared with control mice arbitrarily set at 100.
[c] By two-sided log-rank test on survival curves versus control mice.
[d] Tumor volume inhibition (TVI)% in treated over control mice, assessed 7 days after last treatment.
[e] Body weight loss (BWL), % induced by treatment; the highest observed variation is reported.
[f] Dead/treated mice.
[g] By student's t test versus control tumor volumes.
[h] Not statistically significant.

currently being studied. A similar behaviour in vivo was observed treating Smac mimetic-resistant, human pancreatic carcinoma MIA PaCa-2 cells with dimeric Smac mimetics.[29,30] Smac mimetic-induced production of cytokines such as TNFα was postulated to justify the experimental observations.

Results from both models are summarized in Table 3, showing a promising antitumor effect for lead compound **9a**. A more detailed paper dealing with these and other experiments performed on **9a** will appear elsewhere.[31]

As to future experiments, an analysis of the determinants of tumor response to compounds **9a** and **7** in MDA-MB-231 and IGROV-1 xenograft models will be useful in an attempt to design therapeutic antitumor strategies for advanced stage diseases. We will test **9a** in models implying other therapeutically relevant tumor cell lines, to enlarge its scope as a single agent. Compound **9a** will be administered in a few experimental models together with other cytotoxic agents, to evaluate its potential in combination therapies. Finally, a rigorous toxicological evaluation of compound **9a**, including MTD determination, is planned.

11. Conclusions

In this Letter we report the biological and structural characterization of twenty 1-aza-2-oxobicyclo[5.3.0]decanes as dimeric Smac mimetics, including nine head–head homodimers (**8a–i**), seven tail–tail homodimers (**9a–g**) and four head–tail heterodimers (**10a–d**). The compounds were rationally designed to determine how bifunctional inhibitors of XIAP and cIAPs interact with their BIR domains, and how dimeric structures—namely linkers and 4-substitutions—influence binding potencies on various constructs.

The compounds were tested for inhibition of BIR3 and linker-BIR2–BIR3 domains, two fragments of the protein XIAP, a popular and validated target in apoptosis/oncology. They were also tested on BIR3 from cIAP-1, another cancer-relevant molecular target. Several compounds exhibited sub-micromolar activities on cIAP-1 BIR3 and-or on XIAP linker-BIR2–BIR3. Best results were obtained for head–head dimer **8i**, for tail–tail dimers **9a–f,h** and for heterodimers **10a–c**. The positive influence of small, polar 4-substitutions such as the hydroxymethyl group in most of dimers **9** and **10** was determined.

Cytotoxicity of dimers **8a**–**10d** was measured on MDA-MB-231 cells. At least one representative from each dimer class was tested on HL-60 and PC-3 cells. The compounds exhibited cellular potencies ranging between 55 nM and >50 μM. Their permeability through cell membranes, and their access to the intracellular site of action should contribute to the observed cytotoxicity values. An examination of the most potent dimers on a wider panel of tumor cell lines may identify additional applications for dimeric Smac mimetics.

A compromise between in vitro potency, stability, solubility and cell permeability was reached in lead compound **9a**. The compound was submitted to a preliminary in vivo evaluation, showing reasonable bioavailability and efficacy in MDA-MB-231 and IGROV-1 xenograft models. Reported data by others on structurally similar dimers[3,9,13,29,30] will help us in targeting our future in vivo efforts on **9a** and on other dimeric Smac mimetics.

Structural theories derived from computational models, STD–NMR experiments, X-ray data and gel filtration tests were presented and discussed. Preliminary structural information on the binding mode of the compounds was gathered, accounting for some target binding differences. Additional experiments, especially on heterodimers **10**, should provide additional, relevant information.

The results presented here will be used to plan and carry out further synthetic, biological and structural activities regarding 4-substituted, 1-aza-2-oxabicyclo[5.3.0]decane-based dimeric Smac mimetics/IAP inhibitors. The identification and characterization of further, potent and selective dimeric Smac mimetics, suitable for preclinical evaluation, is a meaningful objective for our future efforts.

12. Experimental section

12.1. In vitro biology profiling

12.1.1. Fluorescence polarization assay—XIAP BIR3—cloning, expression and purification

A pET28 vector (Novagen) with the cDNA coding for human XIAP BIR3 domain from residue 241 to 356 was used to transform *Escherichia coli* strain BL21. Protein expression was induced by adding isopropyl-β-D-thiogalactopyranoside (IPTG) to a final concentration of 1 mM and 100 μM zinc acetate (ZnAc) for 3 h at 37 °C. Bacteria grown in 2YT medium plus kanamycin were harvested, resuspended in a buffer containing 50 mM Tris HCl pH 7.5, 200 μM NaCl and protease inhibitors, treated with 100 μg/mL lysozyme for 30 min in ice and then lysed by sonication. After elimination of debris by centrifugation, the recombinant protein was purified using Ni-NTA (His-trap Ffcrude, Ge-Healthcare) followed by gel filtration (Superdex 200, Ge-Healthcare). BIR3-Histag was eluted with 250 mM imidazole and thereafter stored in 20 mM Tris pH 7.5, 200 mM NaCl and 10 mM Dithiothreitol.

12.1.2. Fluorescence polarization assay—XIAP BIR3—saturation binding experiments

Fluorescent polarization experiments were performed in black, flat-bottom 96-well microplates (Greiner Bio-One) and fluorescent polarization was measured by Ultra plate reader (Tecan). Fluorescent-labelled Smac peptide [AbuRPF-K(5-Fam)-NH_2] (FITC–SMAC) to a final concentration of 5 nM and increasing concentration of BIR3-His-tag from 0 to 20 μM were added to an assay buffer. The final volume in each well was 120 μL, with the assay buffer consisting of 100 mM potassium phosphate, pH 7.5; 100 μg/mL bovine γ-globulin; 0.02% sodium azide. After a 15 min shaking, the plate was incubated for 3 h at room temperature. Fluorescence polarization was measured at an excitation and emission wavelengths of 485 nm and 530 nm respectively. The equilibrium binding graphs were constructed by plotting millipolarization units (mP) as function of the XIAP BIR3 concentration. Data were analyzed using Prism 5.02 software (Graphpad Software).

12.1.3. Fluorescence polarization assay—XIAP BIR3—competitive binding experiments

Dimers were evaluated for their ability to displace FITC–SMAC probe from recombinant protein. 5 nM of FITC–SMAC, XIAP BIR3-His-tag and serial dilutions of the dimers (concentrations ranging from 4 μM to 0.4 nM) were added to each well to a final volume of 120 μL in the assay buffer described above. The concentration of BIR3-His-tag used was 60 nM, able to bind more than 50% of the ligand in the saturation binding experiment. After being mixed for 15 min on a shaker and incubated 3 h at room temperature, fluorescent polarization was measured by Ultra plate reader (Tecan). All dimers and the fluorescent peptide were stocked in DMSO.

12.1.4. Fluorescence polarization assay—cloning, expression and purification of human cIAP-1 BIR3

The sequence coding for cIAP-1 domain residues 245–357 was cloned in pET21(a) vector (Novagen) with a C-terminal 6xHis-tag. The plasmid was used to transform Escherichia coli strain BL21(DE3). The recombinant protein was purified using Ni-NTA (His-trap FFcrude, Ge-Healthcare), followed by gel filtration

(Superdex 200, Ge-Healthcare). The recombinant protein was eluted in 20 mM Tris pH 8.0, 250 mM NaCl and 10 mM DTT.

12.1.5. Fluorescence polarization assay—cIAP1 BIR3—saturation binding experiments

Fluorescent polarization experiments were performed in black, flat-bottom 96-well microplates (Greiner Bio-One) and fluorescent polarization was measured by Ultra plate reader (Tecan). Fluorescent-labelled Smac peptide [AbuRPF-K(5-Fam)-NH_2] (FITC-SMAC) to a final concentration of 2 nM and increasing concentration of BIR3-His-tag from 0 to 20 μM were added to an assay buffer. The final volume in each well was 120 μL, with the assay buffer consisting of 100 mM potassium phosphate, pH 7.5; 100 μg/mL bovine γ-globulin; 0.02% sodium azide. After a 15 min shaking, the plate was incubated for 3 h at room temperature. Fluorescence polarization was measured at an excitation and emission wavelengths of 485 nm and 530 nm respectively. The equilibrium binding graphs were constructed by plotting millipolarization units (mP) as function of the cIAP1 BIR3 concentration. Data were analyzed using Prism 5.02 software (Graphpad Software).

12.1.6. Fluorescence polarization assay—cIAP1 BIR3—competitive binding experiments

Dimers were evaluated for their ability to displace FITC–SMAC probe from recombinant protein. 2 nM of FITC–SMAC, cIAP1 BIR3-His-tag and serial dilutions of the dimers (concentrations ranging from 4 μM to 0.4 nM) were added to each well to a final volume of 120 μL in the assay buffer described above. The concentration of BIR3-His-tag used was 10 nM, able to bind more than 50% of the ligand in the saturation binding experiment. After being mixed for 15 min on a shaker and incubated 3 h at room temperature, fluorescent polarization was measured by Ultra plate reader (Tecan). All dimers and the fluorescent peptide were stocked in DMSO.

12.1.7. Fluorescence polarization assay—cloning, expression and purification of human XIAP linker-BIR2–BIR3

A pET28 vector (Novagen) with the cDNA coding for human XIAP from residue 124 to 356 (linker-BIR2–BIR3), coding for BIR2 and BIR3 domains and the linker region preceding BIR2, was used to transform *Escherichia coli* strain BL21. Protein expression was induced by adding isopropyl-β-D-thiogalactopyranoside (IPTG) to a final concentration of 1 mM and 100 μM zinc acetate (ZnAc) for 20 h at 20 °C. Bacteria grown in 2YT medium plus kanamycin were harvested, resuspended in a buffer containing 50 mM Tris HCl Ph 7.5, 200 mM NaCl and protease inhibitors, treated with 100 μg/mL lysozyme for 30 min in ice and then lysed by sonication. After elimination of debris by centrifugation, the recombinant protein was purified using Ni-NTA (His-trap Ffcrude, Ge-Healthcare) followed by gel filtration (Superdex 200, Ge-Healthcare). The linker-BIR2–BIR3-His-tag was eluted with 250 mM imidazole and thereafter stored in 20 mM Tris pH 7.5, 200 mM NaCl and 10 mM Dithiothreitol.

12.1.8. Fluorescence polarization assay—XIAP linker-BIR2–BIR3—saturation binding experiments

Fluorescent polarization experiments were performed in black, flat-bottom 96-well microplates (Greiner Bio-One) and fluorescent polarization was measured by Ultra plate reader (Tecan). Fluorescent-labelled dimeric Smac peptide SMAC-1F to a final concentration of 1 nM and increasing concentration of linker-BIR2–BIR3-His-tag from 0 to 2 μM were added to an assay buffer. The final volume in each well was 120 μL, with the assay buffer consisting of 100 mM potassium phosphate, pH 7.5; 100 μg/mL bovine γ-globulin; 0.02% sodium azide. After a 15 min shaking, the plate was incubated for 3 h at room temperature. Fluorescence polarization was measured at an excitation and emission wavelengths of 485 nm and 530 nm respectively. The equilibrium binding graphs were constructed by plotting millipolarization units (mP) as function of the XIAP LINKER-BIR2–BIR3 concentration. Data were analyzed using Prism 5.02 software (Graphpad Software).

12.1.9. Fluorescence polarization assay—XIAP linker-BIR2–BIR3—competitive binding experiments

Dimers were evaluated for their ability to displace SMAC-1F probe from recombinant protein. 1 nM of SMAC-1F, 3 nM of XIAP linker-BIR2–BIR3-His-tag and serial dilutions of the dimers (concentrations ranging from 2 μM to 0.4 nM) were added to each well to a final volume of 120 μL in the assay buffer described above. After being mixed for 15 min on a shaker and incubated 3 h at room temperature, fluorescent polarization was measured by Ultra plate reader (Tecan). All dimers and the fluorescent peptide were stocked in DMSO.

12.1.10. Cellular cytotoxicity assays—cell lines

The human breast epithelial adenocarcinoma cell line MDA-MB-231, the human promyelocytic HL60 cell line and the prostatic adenocarcinoma PC3 cell line were all obtained from Interlab Cell Line Collection (ICLC, Genova, Italy). The cell lines were cultured in RPMI 1640 medium supplemented with 2 mM L-glutamine, Penicillin (100 U/mL) /Streptomycin (100 μg/mL), 10% Fetal Bovine Serum (FBS) (all from Sigma, Milan, Italy) at 37 °C and 5% CO_2 in fully humidified atmosphere. A sub-cultivation ratio of 1:4 was used. Dimers were dissolved in dimethylsulfoxide (DMSO) (Sigma) to obtain a 10 mM solution stored at −20 °C. Drug stocks were diluted with phosphate buffer (PBS) (Sigma) prior to their use.

12.1.11. Cellular cytotoxicity assays—experimental protocols

MDA-MB231 and PC3 cells were seeded in 96-well flat bottom cell culture plates at a density of 5000 cells/well while HL60 cells were seeded at a density of 10,000 cells/well in 100 μL of complete culture medium. MDA-MB-231 and PC3 cells were allowed to adhere for 24 h prior to be exposed to the compounds for 96 h in the incubator. Cells were treated with escalating doses of dimers, ranging from 0.1 nM to 50 μM for up to 72 h. The effect of dimers on cell growth was evaluated by means of a colorimetric assay for the quantification of cell proliferation and viability based on the cleavage of the WST-8 tetrazolium salt by mitochondrial dehydrogenases in viable cells (Promokine, Milan, Italy). WST-8 produces a water-soluble formazan which dissolves directly into the culture medium, eliminating the need for an additional solubilization step. WST-8 is more stable, less cytotoxic and more sensitive than the other tetrazolium salts. Briefly, at time 0 and after 72 h-treatment with dimers, 10 μL of WST-8 were added to each of the 96 well culture plates. After 4 h incubation at 37 °C, the absorbance was measured at 450 nm using the microplate reader 1420 VICTOR multilabel counter (EG&G Wallac, Turku, Finland). The data were then expressed as mean percentage of triplicates normalized to the untreated control. The experiments were repeated twice. The IC_{50}, the concentration of compound capable of inhibiting the cell growth by 50%, was calculated using the GraphPad Prism 4 software.

12.2. Structural studies

12.2.1. Computational methods—Construction of dimeric Smac mimetics/linker-BIR2–BIR3 complexes

Molecular modeling of compounds **8e** and **9a** in complex with XIAP containing BIR2 and BIR3 domains was carried out using the Schrödinger suite of programs (www.schrodinger.com) through the Maestro graphical interface.[32] Computational 3D models of the linker-BIR2–BIR3 construct from XIAP (residues 127–345) in complex with the head–head dimer **8e** or the tail–tail

dimer **9a** were built using the crystal structure of the cyclic, bivalent Smac mimic **6** in complex with the XIAP BIR3 domain (PDB entry 2VSL)[14,15] and the crystal structure of the XIAP BIR2 domain in complex with caspase 3 (PDB entry 1I30, subunit E).[14,16] The intermolecular crystallographic XIAP-BIR3 dimer of PDB entry 2VSL was used as template for the linker-BIR2–BIR3 structure generation. In the modelling, one BIR3 monomer was replaced with a BIR2 molecule (F127-I237) after structural alignment using Maestro.[32] The initial model lacked a 12-residue segment (R238-N249) that connects the BIR2 and BIR3 domains in the native protein. As previously described,[14] the missing segment was incorporated into the model, using a loop from the XIAP-BIR3 NMR structure (PDB entry 1TFQ), in which the loop segment S241-N249 was determined. After alignment and rotation procedures aimed to bring I237 close to S241, the three additional missing residues were added. Dimeric Smac mimetics **8e** and **9a** were placed in this structure of the linker-BIR2–BIR3 construct by alignment of the two AVPI peptidomimetic subunits to the corresponding tetrapeptide motifs of the cyclic, bivalent Smac mimic **6**. The resulting complexes were used as starting structures for explicit solvent extensive molecular dynamics simulations.

12.2.2. Computational methods—Molecular dynamics simulations

MD simulations were performed using the AMBER 9.0 package[17] with the ff03 force field, under periodic boundary conditions. In order to remove any bad contacts, every complex was initially minimized in vacuo by multiple minimizations (200 steps steepest descent plus 200 steps conjugate gradient). After this, each system was solvated in a cubic box large enough to contain 1 nm of solvent molecules around the complex. The TIP3P water model was used for solvation.[33] Charges on side chains were chosen to correspond to a pH value of 7. Na+ counterions were added to ensure electroneutrality. In order to allow the solvent molecules to relax around the solute the system was minimized keeping the complex fixed and just minimizing the positions of water and ions (500 steps steepest descent plus 200 steps conjugate gradient); a cut-off of 1 nm was used to compute the non-bonded interactions. Particle Mesh Ewald summation method (PME) was used to deal with long-range Coulomb interactions.[34] The Berendsen's algorithm was used to control temperature and pressure.[35] After this minimization stage holding the solute fixed, the entire system was energy minimized (1500 steps steepest descent plus 1000 steps conjugate gradient). Afterwards, the temperature of the system was slowly brought to the desired value of 300 K using a weak restrain on the solute at constant volume in order to avoid any fluctuations. Finally, a last 100 ps equilibration NPT process was performed with no restrictions on the system. This protocol resulted in 30 ns MD runs for **8e** complex and 50 ns MD runs for **9a** complex. In the XIAP protein a zinc ion is coordinated to three cysteines and one histidine. The zinc ion was treated using the cationic dummy approach.[36] This method consists in modeling the zinc ion as a tetrahedral divalent cation with a zinc nucleus and four dummy atoms placed at the four apices of the tetrahedron, in order to impose the right orientation required for the coordinated residues. The zinc atom is bound covalently to the dummy atoms and interacts with the protein only through van der Waals forces, while the dummies interact with the protein only through electrostatic forces. Parameters used to describe the metal and dummies, their charge and bonding properties are detailed elsewhere.[36]

12.2.3. NMR–STD experiments

All protein construct/ligand samples were prepared in a 1:60 construct/ligand ratio. Typically, the final concentration of the samples was 7 mM in Smac mimic and 0.11 mM in proteins, and the final volume was 200 μL. The buffer used for protein construct samples was 100 mM NaCl, 10 mM deuterated Tris, 5 mM deuterated DTT in D_2O, pH 7.3. ^1H NMR–STD experiments were performed at 600 MHz on a Bruker Avance spectrometer. The probe temperature was maintained at 298 K using the STD sequence of the Bruker library. The on-resonance irradiation of the protein was performed at a chemical shift of −0.05 ppm. Off-resonance irradiation was applied at 200 ppm, where no protein signals were visible. Selective pre-saturation of the protein was achieved by a train of Gauss shaped pulses of 49 ms length each. The total length of the saturation train was 2.94 s.

12.2.4. Crystallographic methods

Crystals of the different XIAP BIR3 complexes were grown by vapour diffusion methods as co-crystallizations, as previously[19] and otherwise[25] described. The crystal structure of the XIAP BIR3 complex with compound **5** was solved by molecular replacement and refined at 3.0 Å (PDB code 3G76) as previously described.[19] The crystal structure of the XIAP BIR3 complex with compound **9a** will be described in details elsewhere.[25]

12.2.5. Gel filtration

Analytical gel-filtration experiments were performed with a Superdex 75 column (GE Healthcare) coupled to an AKTA Purifier system using 20 mMTris–HCl pH 7.5, 200 mM NaCl, 10 mM DTT. Recombinant XIAP-BIR2BIR3 was run on the column at a concentration of 1 mg/mL, either alone or after incubation for 30 min with an excess of dimeric compounds (5 mM).

12.2.6. SAXS

X-ray scattering data were collected at the beamline SWING of Synchrotron SOLEIL (Gif-sur-Yvette, France). The data were recorded using a CCD-based detector (AVIEX) with a sample-detector distance of 2.07 m, covering the range of momentum transfer $0.010 < q < 0.45$ Å^{-1} ($q = 4\pi$ sinql, where 2q is the scattering angle and $\lambda = 1.033$ Å the wavelength of the X-rays). XIAP-BIR2–BIR3 with and without the inhibitor **9a** was studied in Tris–HCl buffer 20 mM pH 7.5, NaCl 200 mM and DTT 10 mM at protein concentrations between 1 and 7 mg/mL as described elsewhere.[25] All measurements were performed at 10 °C. Data were averaged after normalization to the intensity of the transmitted beam before buffer subtraction using the program package PRIMUS.[37] The forward scattering *I(0)* and the radius of gyration (R_g) were evaluated using the Guinier approximation[38] as previously described.[19]

12.3. In vivo studies

12.3.1. Pharmacokinetics—general settings

Male CD-1 mice (body weights 20–25 g at the time of the supply) were used in this study. The animals were originally supplied by Charles River Italy, Calco. Once received in house, the animals were subjected to health examinations and acceptance. The animals were housed, in a group of 5, in suitable cages, also during dosing and feeding periods. The animals were acclimatized to local housing conditions for approximately 5 days and routinely kept in the following environment, except for short periods of time where experimental procedures dictated otherwise. The animals were housed in a single, air conditioned room, to provide a minimum of 13 air changes/hour. The environmental controls were set to maintain temperature within the range 19 to 24 °C and relative humidity within the range 50 to 60%, with an approximate 12 h light and 12 h dark cycle that was automatically monitored. Food (Mucedola Standard GLP diet) and water were available ad libitum throughout the study. The diet and water supplied to the animals were routinely analysed, with no contaminants in either the diet or water that were considered to potentially affect the integrity or outcome of the study. All the animals were weighed on the

day of the treatment, and were uniquely identified with a number before the experiment. Clinical signs were monitored at regular intervals throughout the study in order to assess any reaction to treatment.

12.3.2. Pharmacokinetics—ip route of administration

Mice were treated with **9a** by intraperitoneal admininistration and sacrificed at eight time points (5, 15, 30, 60, 120, 240, 480 min and 24 h) under anesthesia with ethyl ether. Blood (about 500 μL) was collected in heparinized tubes, and centrifuged (3500 × g, 15 min, 4 °C). Plasma samples were stored at −80 °C and later analyzed by LC–MS/MS (Premiere XE, Waters) at the analytical conditions set up for **9a**. The LLOQ (Lowest Limit Of Quantification) was 1 ng/mL.

12.3.3. Pharmacokinetics—iv route of administration

Mice were treated with **9a** by intravenous administration and sacrificed at eight time points (2, 10, 30, 60, 120, 240, 480 min and 24 h) under anesthesia with ethyl ether. Blood (about 500 μL) was collected in heparinized tubes, and centrifuged (3500 × g, 15 min, 4 °C). Plasma samples were stored at −80 °C and later analyzed by LC–MS/MS (Premiere XE, Waters) at the analytical conditions set up for **9a**. The LLOQ (Lowest Limit Of Quantification) was 1 ng/mL.

12.3.4. Efficacy studies—MDA-MB-231—Tumor xenografts— ip/sc

Exponentially growing tumor cells (5×10^6 cells/mouse) were sc injected into the right flank of NOD/SCID mice. Mice were maintained in laminar flow rooms keeping temperature and humidity constant. Mice had free access to food and water. Experiments were approved by the Ethics Committee for Animal Experimentation of the Istituto Nazionale Tumori of Milan according to institutional guidelines. Groups of four mice bearing bilateral sc tumors were employed. Cells were transplanted and tumor growth was evaluated by biweekly measurements of tumor diameters with a Vernier caliper. Tumor volume (TV) was calculated according to the formula: TV (mm^3) = $d^2 \times D/2$ where d and D are the shortest and the longest diameter, respectively. Compound **9a** was delivered ip and administered 5 days a week for three weeks (qdx5/wx3w). Treatment started fourteen days after tumor implant and efficacy of the drug was assessed as tumor volume inhibition percentage (TVI%) in treated versus control mice, calculated as: TVI% = 100−(mean TV treated/mean TV control × 100). The toxicity of the drug treatment was determined as body weight loss and lethal toxicity. Student *t* test (two tailed) was used for statistical comparison of tumor volumes.

12.3.5. Efficacy studies—IGROV-1—general settings

All experiments of antitumor activity were carried out using female athymic Swiss nude mice, 8–10 weeks-old (Charles River, Calco, Italy). Mice were maintained in laminar flow rooms keeping temperature and humidity constant. Mice had free access to food and water. Experiments were approved by the Ethics Committee for Animal Experimentation of the Istituto Nazionale Tumori of Milan according to institutional guidelines. The IGROV-1 human ovarian tumor xenograft derived from an ovarian carcinoma cell line obtained from an untreated patient was used in the study. Compound **9a** was dissolved in saline at a concentration of 0.5 mg/ml, whereas standard dimer **7** was dissolved in a mixture of ethanol and cremophor employing a magnetic stirrer and suspended in saline at a final concentration of 5 + 5 + 90%. The drugs were freshly dissolved at the beginning of the weekly administration following analysis of stability by HPLC–MS, which under the present conditions was maintained up to 5 days. The drugs were delivered ip in a volume of 10 ml/Kg of body weight.

12.3.6. Efficacy studies—IGROV-1—Tumor xenografts—ip

The IGROV-1 tumor was adapted to grow in the peritoneal cavity (ip) and maintained by serial ip passages of ascitic cells into healthy mice. In this tumor model, hemorrhagic ascites with diffuse peritoneal carcinomatosis develop and the animal eventually die. For evaluation of antitumor activity, 2.5×10^6 ascitic cells in 0.2 mL of saline were injected ip into mice. Locoregional administration was employed. In particular, treatments started 1 day after cell inoculum. Compounds **9a** and **5** were delivered ip at a dose of 5 mg/Kg and administered for 4–5 days a week for two weeks (qdx4-5/wx2w), starting the day after cell injection. For antitumor activity studies, experimental groups were inspected daily and weighed three times weekly. Prior to impending death, mice were sacrificed by cervical dislocation and day of sacrifice was considered as day of death and the median survival time (MST) was calculated for each group. Antitumor activity was assessed as T/C%, i.e., the ratio of MST in treated mice over that of control mice × 100. For statistical analysis, percent survivorship over time was estimated by the Kaplan–Meier product method and compared using the log-rank test.

12.3.7. Efficacy studies—IGROV-1—Tumor xenografts—ip/sc

For subcutaneous (sc) growth, exponentially growing tumor cells (5×10^6 cells/mouse) were sc injected into the right flank of athymic nude mice. The tumor line was achieved by serial sc passages of fragments (about 2 × 2 × 6 mm) from regrowing tumors into healthy mice. Groups of five mice bearing bilateral sc tumors were employed. Tumor fragments were implanted on day 0 and tumor growth was followed by biweekly measurements of tumor diameters with a Vernier caliper. Tumor volume (TV) was calculated according to the formula: TV (mm^3) = $d^2 \times D/2$ where d and D are the shortest and the longest diameter, respectively. Compounds **9a** and **7** were delivered ip and administered for 5 days a week for three weeks (qdx5/wx3w). Treatment started three days after tumor implant, when tumors were just palpable. The efficacy of the drug treatment was assessed as tumor volume inhibition percentage (TVI%) in treated versus control mice, calculated as: TVI% = 100−(mean TV treated/mean TV control × 100). The toxicity of the drug treatment was determined as body weight loss and lethal toxicity. Deaths occurring in treated mice before the death of the first control mouse were ascribed to toxic effects. Student t test (two tailed) exact test was used for statistical comparison of tumor volumes in mice.

Acknowledgments

The authors are thankful to 'FONDAZIONE CARIPLO' for financing through Project 2009-2534, titled '*Inhibitors of Apoptosis Proteins (IAPs) as anticancer therapeutics*', and to 'ASSOCIAZIONE ITALIANA PER LA RICERCA SUL CANCRO' (AIRC) for financing through Project 2010-9998, titled '*Special Program—Molecular Clinical Oncology—5 per mille*'.

References and notes

1. Manzoni, L.; Belvisi, L.; Bianchi, A.; Conti, A.; de Matteo, M.; Drago, C.; Ferrante, L.; Mastrangelo, E.; Manzoni, L.; Perego, P.; Potenza, D.; Scolastico, C.; Servida, F.; Timpano, G.; Vasile, F.; Rizzo, V.; Seneci, P. *Bioorg. Med. Chem.* **2012**. http://dx.doi.org/10.1016/j.bmc.2012.09.020.
2. Li, L.; Thomas, R. M.; Suzuki, H.; De Brabander, J. K.; Wang, X.; Harran, P. G. *Science* **2004**, *305*, 1471.
3. Lu, J.; Bai, L.; Sun, H.; Nikolovska-Coleska, Z.; McEachern, D.; Qiu, S.; Miller, R. S.; Yi, H.; Shangary, S.; Sun, Y.; Meagher, J. L.; Stuckey, J. A.; Wang, S. *Cancer Res.* **2008**, *68*, 9384.
4. Nikolovska-Coleska, Z.; Wang, R.; Fang, X.; Pan, H.; Tomita, Y.; Li, P.; Roller, P. P.; Krajewski, K.; Saito, N. G.; Stuckey, J. A.; Wang, S. *Anal. Biochem.* **2004**, *332*, 261.
5. Nikolovska-Coleska, Z.; Meagher, J. L.; Jiang, S.; Kawamoto, S. A.; Gao, W.; Yi, H.; Qin, D.; Roller, P. P.; Stuckey, J. A.; Wang, S. *Anal. Biochem.* **2008**, *374*, 87.

6. Mastrangelo, E.; Cossu, F.; Milani, M.; Sorrentino, G.; Lecis, D.; Delia, D.; Manzoni, L.; Drago, C.; Seneci, P.; Scolastico, C.; Rizzo, V.; Bolognesi, M. *J. Mol. Biol.* **2008**, *384*, 673.
7. Ndubaku, C.; Varfolomeev, E.; Wang, L.; Zobel, K.; Lau, K.; Elliott, L. O.; Maurer, B.; Fedorova, A. V.; Dynek, J. N.; Koehler, M.; Hymowitz, S. G.; Tsui, V.; Deshayes, K.; Fairbrother, W. J.; Flygare, J. A.; Vucic, D. *ACS Chem. Biol.* **2009**, *4*, 557.
8. Peng, Y.; Nikolovska-Coleska, Z.; Qin, D.; Sun, H.; Yang, C.-Y.; Bai, L.; Qiu, S.; Wang, Y.; Ma, D.; Wang, S. *J. Med. Chem.* **2009**, *52*, 593.
9. Peng, Y.; Sun, H.; Lu, J.; Liu, L.; Cai, Q.; Shen, R.; Yang, C.-Y.; Yi, H.; Wang, S. *J. Med. Chem.* **2012**, *55*, 106.
10. Sun, H.; Nikolovska-Coleska, Z.; Lu, J.; Meagher, J. L.; Yang, C.-Y.; Qiu, S.; Tomita, Y.; Ueda, Y.; Jiang, S.; Krajewski, K.; Roller, P. P.; Stuckey, J. A.; Wang, S. *J. Am. Chem. Soc.* **2007**, *129*, 15279.
11. Lecis, D.; Drago, C.; Manzoni, L.; Seneci, P.; Scolastico, C.; Mastrangelo, E.; Bolognesi, M.; Anichini, A.; Kashkar, H.; Walczak, H.; Delia, D. *Br. J. Cancer* **2010**, *102*, 1707.
12. Shonberg, J.; Scammels, P. J.; Capuano, B. *ChemMedChem* **2011**, *6*, 963.
13. Sun, H.; Liu, J.; Lu, J.; Bai, L.; Li, X.; Nikolovska-Coleska, Z.; McEachern, D.; Yang, C.-Y.; Qiu, S.; Yi, H.; Sun, D.; Wang, S. *J. Med. Chem.* **2011**, *54*, 3306.
14. www.pdb.org
15. Nikolovska-Coleska, Z.; Meagher, J. L.; Jiang, S.; Yang, C.-Y.; Qiu, S.; Roller, P. P.; Stuckey, J. A.; Wang, S. *Biochemistry* **2008**, *47*, 9811.
16. Riedl, S. J.; Renatus, M.; Schwarzenbacher, R.; Zhou, Q.; Sun, C.; Fesik, S. W.; Liddington, R. C.; Salvesen, G. S. *Cell* **2001**, *104*, 791.
17. Case, D.A.; Darden, T.A.; Cheatham, III, T.E.; Simmerling, C.L.; Wang, J.; Duke, R.E.; Luo, R.; Merz, K.M.; Pearlman, D.A.; Crowley, M.; Walker, R.C.; Zhang, W.; Wang, B.; Hayik, S.; Roitberg, A.; Seabra, G.; Wong, K.F.; Paesani, F.; Wu, X.; Brozell, S.; Tsui, V.; Gohlke, H.; Yang, L.; Tan, C.; Mongan, J.; Hornak, V.; Cui, G.; Beroza, P.; Mathews, D.H.; Schafmeister, C.; Ross, W.S.; Kollman, P.A. AMBER 9, 2006, University of California.
18. Gyration radius mean values of 21.5 Å and 22.0 Å have been calculated for the protein structures sampled during the simulations with compound **8e** and **9a**, respectively.
19. Wu, G.; Chai, J.; Suber, T. L.; Wu, J. W.; Du, C.; Wang, X.; Shi, Y. *Nature* **2000**, *1008*, 408.
20. Cossu, F.; Mastrangelo, E.; Milani, M.; Sorrentino, G.; Lecis, D.; Delia, D.; Manzoni, L.; Seneci, P.; Scolastico, C.; Bolognesi, M. *Biochem. Biophys. Res. Commun.* **2008**, *378*, 162.
21. Potenza, D.; Belvisi, L.; Vasile, F.; Moroni, E.; Cossu, F.; Seneci, P. *Org. Biomol. Chem.* **2012**, *10*, 3278.
22. A distance cutoff of 4.0 Å for donor hydrogen–acceptor heteroatom distance has been used to calculate this percentage on conformations sampled during the simulation.
23. Meyer, B.; Peters, T. *Angew. Chem., Int. Ed.* **2003**, *42*, 864.
24. Mayer, M.; Meyer, B. *J. Am. Chem. Soc.* **2001**, *123*, 6108.
25. Cossu, F.; Milani, M.; Vachette, P.; Malvezzi F.; Grassi, S.; Canevari, G.; Lecis, D.; Delia, D.; Drago, C.; Seneci, P.F.; Bolognesi, M.; Mastrangelo, E. *manuscript in preparation*.
26. Qualitative estimation of oral bioavailability in a $CaCO_2$, early ADMET assay for dimers **8e** and **9a** showed extremely low permeability (unpublished results).
27. Romanelli, S.; Perego, P.; Pratesi, G.; Carenini, N.; Tortoreto, M.; Zunino, F. *Cancer Chemother. Pharmacol.* **1998**, *41*, 385.
28. Pratesi, G.; Tortoreto, M.; Corti, C.; Giardini, R.; Zunino, F. *Br. J. Cancer* **1995**, *71*, 525.
29. Dineen, S. P.; Roland, C. L.; Greer, R.; Carbon, J. G.; Toombs, J. E.; Gupta, P.; Bardeesy, N.; Sun, H.; Williams, N.; Minna, J. D.; Brekken, R. A. *Cancer Res.* **2010**, *70*, 2852.
30. Probst, B. L.; Liu, L.; Ramesh, V.; Sun, H.; Minna, J. D.; Wang, L. *Cell Death Differ.* **2010**, *17*, 1645.
31. Perego, P; Lecis, D.; Delia, D. et al. Org. Biomol. Chem., *manuscript in preparation*.
32. Maestro, version 8.0, Schrödinger, LLC, New York, NY, 2007.
33. Jorgensen, W. L.; Chandrasekhar, J.; Madura, J.; Impey, R. W.; Klein, M. L. *Chem. Phys.* **1983**, *79*, 926.
34. Darden, T.; York, D.; Pedersen, L. *J. Chem. Phys.* **1993**, *98*, 10089.
35. Berendsen, H. J. C.; Postma, J. P. M.; Gunsteren, W. F.; Nola, A. D.; Haak, J. R. *J. Chem. Phys.* **1984**, *81*, 3684.
36. Pang, Y.; Xu, K.; El Yazla, J.; Prendergast, F. *Protein Sci.* **1857**, *2000*, 9.
37. Konarev, P. V.; Volkov, V. V.; Sokolova, A. V.; Koch, M. H. J.; Svergun, D. I. *J. Appl. Crystallogr.* **2003**, *36*, 1277.
38. Guinier, A. *Ann. Phys. (Paris)* **1939**, *12*, 161.